International Journal of Nanoelectronics and Materials

In Press, Accepted Manuscript – Note to user

The Impact of Stress Distribution on The Electrical Performance of Different Silver Stretchable Conductive Ink Pattern Using FEA Simulation

Daniel Azlan Bin Mohd Azli[1], Mizah Binti Ramli[1,2], Mohamad Shukri Bin Zakaria[1,2], Mohd Nur Azmi Bin Nordin[1,2], Ghazali Bin Omar[1] Mariam Binti Md Ghazaly[3] and Abdul Halim Lim Bin Abdullah[4]

[1]Fakulti Kejuruteraan Mekanikal, Universiti Teknikal Malaysia Melaka, Hang Tuah Jaya, 76100 Durian Tunggal Melaka, Malaysia
[2]Centre for Advanced Research on Energy (CARE), Universiti Teknikal Malaysia Melaka, Hang Tuah Jaya, 76100 Durian Tunggal, Melaka, Malaysia
[3] Fakulti Kejuruteraan Elektrikal, Universiti Teknikal Malaysia Melaka, Hang Tuah Jaya, 76100 Durian Tunggal Melaka, Malaysia
[4] Top Empire Sdn. Bhd., Lot 16037, Jalan Teknologi 6, Kawasan Perindustrian Tangkak, 84900 Tangkak, Johor, Malaysia

Received 6 April 2022, Revised 23 May 2022, Accepted 14 June 2022

ABSTRACT

Stretchable conductive ink has been widely investigated to be used in the fabrication of stretchable electrical devices. Experimentation methods to test the mechanical and electrical behaviours of the stretchable conductive ink composite are commonly applied; however, not much of the computational approach has been scrutinized to validate the results further. This paper employs the finite element analysis method to investigate the relationship between the stress and strain distribution of the stretchable conductive ink with the highest strain obtained. This research validates the past experimentation works of different patterns of stretchable conductive ink for its stretchability and electrical performance. The maximum Von Mises stress (VMS) and maximum principal strain of the stretchable conductive ink played a significant role in determining its electrical performance, rather than the localisation of high stress and strain at specific locations within the stretchable conductive ink pattern. Zigzag pattern exhibited the lowest maximum stress and strain concentration at 57.826 MPa and 4.05% while straight pattern suffered the highest respective values at 118.143 MPa and 10.39%. The lower maximum Von-Mises stress and principal strain contributed to a better stretchability which is indicated by a higher strain rate prior to electrical conductivity.

Keywords: stress distribution analysis, strain distribution analysis, FEA, SCI, stretchability.

1. INTRODUCTION

The electronics industry has experienced a paradigm change in recent years toward developing both flexible and stretchable devices [1]. Flexible and printable electronics have received considerable interest and are generally regarded as the electronic industry's future [2]. A stretchable electronic circuit (SEC) is a technique developed to boost the flexibility, twistability, and stretchability of a rigid printed circuit board (PCB) [3].

In contrast, a conductive circuit is a critical component of PCB. As it goes by the name, stretchable conductive ink (SCI) is a type of ink that is able to stretch while maintaining its electrical conductivity. SCI is the primary component of SEC [4]. The SCI composite must include some kind

* Corresponding Author: mizah@utem.edu.my

of conductive filler as the dispersed phase to be conductive. SCI is used to assess the composite's electrical or thermal conductivity and its ability to stretch or flex, which varies based on the type of conductive filler used. Numerous kinds of conductive fillers are shown in the laboratory [5]–[7] as well for commercial usage [8], [9]. Silver (Ag), gold (Au), and copper (Cu) nanoparticles are presently the most often used conductive fillers. The silver nanoparticle is often used as a conductive ink filler to increase the ink's conductivity since it has the most excellent electrical conductivity of all metal-based fillers [10]. However, the experimentation technique may be expensive owing to the need to repeat each experiment to get normalised or averaged data. Unlike experimental method, the growth of universal or local stress and strain resulted from external applied force can be calculated through computational simulation method. Thus, this method can be used to access the development of both stress and strain level within the SCI under various mechanical loadings.

Along with experimental procedures, numerical techniques based on digital computers are becoming a viable option. The numerical methods for structural analysis are classified into three categories: the long-established but limited capability finite difference method, the finite element method (developed from earlier structural matrix methods), which gained popularity in the 1950s with the advent of digital computers, and the boundary element method, which emerged more than a decade later [11]. The primary goal of computer analysis is to validate experimental research rather than totally replace it, since the experimental findings may be the input parameters for the computational approach. In this study, a stress distribution analysis of Ag SCI will be conducted to validate the experimental result [1] through the finite element analysis (FEA) method by using Abaqus software. It was shown that different interconnect shapes may offer various ranges of stretchability as they influence the development of other stress and strain levels within [12]–[14]. Patterns of straight, square, sinusoidal, and zigzag are employed to evaluate each pattern's stress and strain distribution when subjected to different uniaxial loadings and biaxial loading. From the experiment, in terms of maximum elongation percentage before the ink started to lose conductivity, the zigzag line pattern showed the best result, following sinusoidal, square, and lastly straight pattern as shown in Table 1 [1].

Table 1. Maximum elongation rate before each pattern starts losing its conductivity [1]

Pattern	Maximum Strain (%)
Straight	1.11
Square	3.33
Sinusoidal	6.67
Zigzag	7.78

2. METHODOLOGY

Finite element analysis (FEA) is the process of modelling the behaviour of a component or assembly under specified conditions to evaluate it using the finite element method (FEM). The results obtained through simulation were captured in the "Visualization" module, readily for view in both contour and symbol plot. Abaqus' output database offers multitude output types, including Von Mises Stress (VMS) and maximum principal strain. Theoretically, a material with lower VMS will fracture earlier under the same loading condition relatively to a material possessing higher VMS value. The same logical assessment can be applied for the principal strain, whereby a material having a higher maximum principal strain is assumed to yield earlier at the same loading condition compared to a material with relatively lower maximum principal strain. Thus, the effect of having different patterns of SCI interconnect can be accessed by evaluating the values of stress and strain for each of the patterns used.

There were four patterns used in this study to analyse the VMS and the maximum principal strain of the SCI. Abaqus automatically displays the VMS constant stress tensor curve as a default. When a material's plastic yielding is present, this amount is quite helpful. VMS is a formula that combines the principal stresses to provide equivalent stress compared to the material's yield stress as denoted in equation 1 [15].

$$(\sigma_1 - \sigma_2)^2 + (\sigma_2 - \sigma_3)^2 + (\sigma_3 - \sigma_1)^2 = 2\sigma_e^2 \quad (1.0)$$

Where σ_1, σ_2, and σ_3 are the principal stresses in the direction of x-, y-, and z-axis respectively, and σ_e is the equilibrium stress

Maximum principal strain theory, also called Saint Venant's theory, is the highest value of significant strain developed in the body that surpasses the limiting value of strain, that is, the strain value corresponding to the yield point of the material causing it to fail. Thus, when the maximum principal strain subjected to a biaxial or triaxial state of stress equals the strain at the yield point of a reference specimen submitted to a basic tensile test, the component fails. For a triaxial loading, let us consider the following parameters. For triaxial loading, these sets of parameters are considered: (i) Young's modulus = E, (ii) Poisson's ratio = μ, (iii) Principal stresses = σ_1, σ_2 and σ_3, and (iv) Principal strains = ϵ_1, ϵ_2 and ϵ_3

Under this loading, it is assumed that "$\epsilon_1 > \epsilon_2 > \epsilon_3$"' and this assumption follows the generalised Hooke's Law concept. Along with the hypothesis, the maximum principal strains can be expressed in terms of principal stresses along with the properties of Young's modulus and Poisson's ratio into the equation 2.0 until 2.2.

$$\epsilon_1 = \frac{\sigma_1}{E} - \mu\frac{\sigma_2}{E} - \mu\frac{\sigma_3}{E}$$

$$\epsilon_1 = \frac{1}{E}[\sigma_1 - \mu(\sigma_2 + \sigma_3)] \quad (2.0)$$

$$\epsilon_2 = \frac{1}{E}[\sigma_2 - \mu(\sigma_3 + \sigma_1)] \quad (2.1)$$

$$\epsilon_3 = \frac{1}{E}[\sigma_3 - \mu(\sigma_1 + \sigma_2)] \quad (2.2)$$

Now, considering standard specimen subjected to uniaxial tension in a simple tensile test, assume that simple specimen has a yield point strain of ϵ_{yt}. Since it is a simple uniaxial loading, we can

apply the simple Hooke's Law, which is $\epsilon_{yt} = \sigma_{yt}/E$. From Saint Venant's Theory, failure will occur when $\epsilon_1 > \epsilon_{yt}$, deriving equation 2.3 and 2.4.

$$\frac{1}{E}[\sigma_1 - \mu(\sigma_2 + \sigma_3)] \geq \frac{\sigma_{yt}}{E} \quad (2.3)$$

Eq. (2.3) can be simplified as: $[\sigma_1 - \mu(\sigma_2 + \sigma_3)] \geq \sigma_{yt}$ (2.4)

For the preliminary testing, a few patterns were developed within the simulation software. The patterns are adapted from the past experimentation works conducted to examine further the effect of in-plane stress and strain distribution on the electrical performance of SCI [1]. The finite element analysis (FEA) simulation upon the patterns was run by Abaqus software. The stretchability of the patterns was evaluated by observing the maximum principal strains and the VMS of the patterns at different locations. The four patterns that were used are straight, sinusoidal, zigzag, and square patterns. The straight line was made as to the baseline patterns for the comparison purpose. Equation 4.0 gives the average stress.

$$\sigma_{avg} = (\sigma_{max} + \sigma_{min})/2 \quad (4.0)$$

Where σ_{avg}, $\sigma_{max,}$ and σ_{min} represent average stress, maximum stress, and minimum stress.

2.1. Model of SCI

As aforementioned, four different patterns were chosen, modelled, and simulated by FEA software further to analyse the stress-strain behaviours of each design. The length of each pattern was set to be 90 mm. The ink's width and thickness were 3 mm and 0.005 mm, respectively. The length, width, and thickness of the substrate were set to be 95 mm, 30 mm, and 0.1 mm, respectively. The dimensions of the modelled pattern within the simulation software were chosen to resemble the dimension of patterns from recent experimental work by Yunos et. Al. [1] to explore the correlation of induced stress and strain to experimental method. All the patterns will be embedded in the middle of the substrate. Figure 1 indicates the general dimension for the model of the pattern for straight-line pattern, and the same measurement is applied to other patterns. Figure 2 denotes the model for other patterns employed in this research viewed from the top.

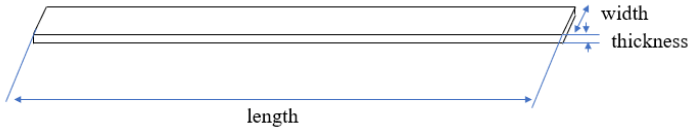

Figure 1. General dimension for the model of SCI pattern

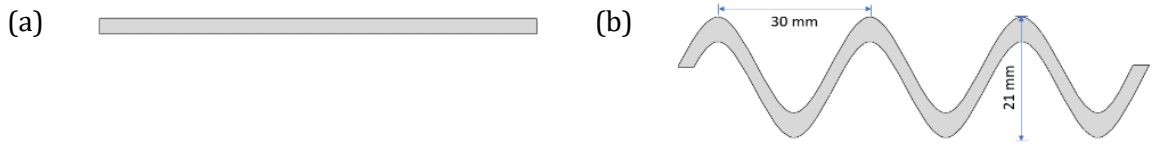

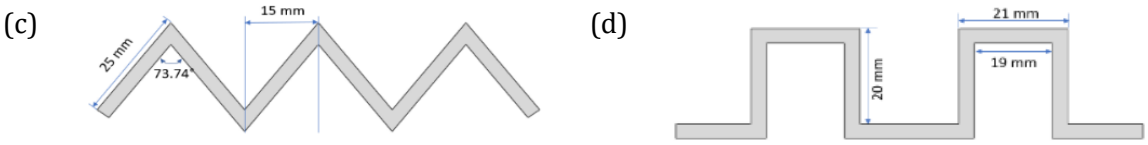

Figure 2. Modelled silver ink patterns of (a) Straight, (b) Sinusoidal, (c) Zigzag, and (d) Square

2.2. Material Properties

The material used as the SCI is silver ink which is a metal nanoparticles filler and thermoplastic urethane (TPU) as the substrate. Mechanical data such as Young's Modulus and Poisson's ratio for the silver ink was obtained from other research employing a similar type of ink and substrate [5]. Table 2 describes the properties of silver ink and TPU substrate implemented in the simulation. The mechanical behavior of the SCI was set to be elastic to observe the stretchability of the SCI when subjected to uniaxial stretching of 10%.

Table 2. Properties of ink and filler used in the simulation

Materials	Properties		
	Young's Modulus (MPa)	Poisson's Ratio	Density (kg/m^3)
Silver ink	1034.21	0.25	2.2×10^3
TPU substrate	11.55	0.45	1.2×10^3

2.3. Mesh Convergence Study

Mesh convergence tests for two patterns, straight and zigzag, were conducted. This test was done to obtain valid results and reduce the computational period, as further increasing the elemental counts will prolong the computational period. Both of the patterns were chosen due to the different meshing densities used—straight patterns employed 0.5 and 1 mm for ink and substrate, respectively. As for zigzag, square, and sinusoidal patterns, 0.7 mm and 1 mm meshing densities were applied for ink and substrate, respectively. However, a zigzag pattern was selected as the representative for square, and a sinusoidal pattern for this test as all three possessed approximately similar elemental counts at 0.7 mm meshing density.

2.4. Boundary Conditions (BC)

Boundary conditions (BC) are limitations that must be met to solve boundary value issues. All the models of silver ink made of different patterns used in the simulation were subjected to uniaxial (longitudinal and lateral) or biaxial loading.

2.4.1. Uniaxial Longitudinal and Lateral Loading

In the model, one of the ends was subjected to a fixed support, while the other was subjected to uniform load, as shown in Figure 3. In this case, the mechanical loadings comprise of elongation stress and strain. For the simulation purpose, three boundary conditions employed to model the patterns, namely BC1, BC2, and BC3, respectively. Figures 3(a) and 3(b) show the model's schematic diagram subjected to the loadings from boundary conditions.

(a)

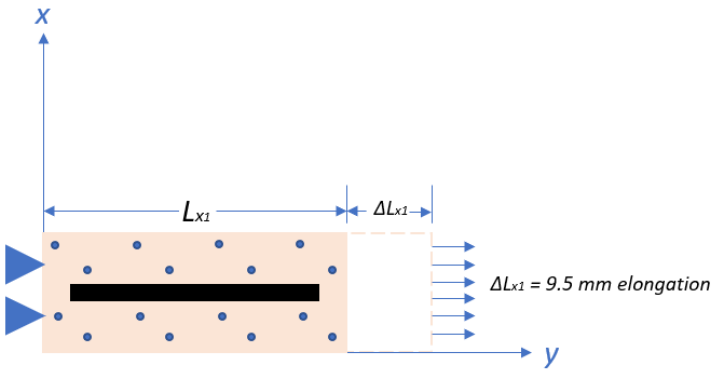

(b)

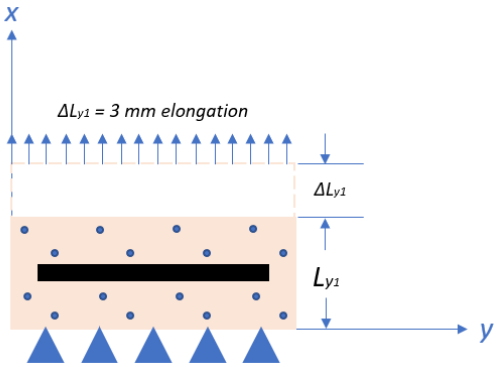

Figure 3. Schematic diagram of the model at the application of BC1, BC2, and BC3 for (a) longitudinal and (b) lateral loading. The fixed end and loading point location is denoted by the triangular shape and arrows, respectively while the dotted lines on the substrate denoted that the surface was constrained from deflection in z-axis. Light red shape denotes the substrate while black shape denotes the ink on top of the substrate. All the patterns employed the same boundary conditions.

BC1 is the fixed end, at x = 0 mm, and y = 0 mm for uniaxial longitudinal and lateral loading, respectively. BC1 was applied normal to the cross-sectional area region of the end (substrate), causing the whole surface area to be constrained in displacement and reaction force. For longitudinal loading, BC1 was set to along y = 0 and along x = 0 for lateral loading.

BC2 covered the whole body of the model, where the entire model was constrained from rotational displacement in all directions and translational displacement normal to the model. Blue dots within Figures 3(a) and 3(b) represent the area of constraint indicated by BC2. Implementing this boundary condition assumes that the model will not deform out-of-plane from the applied elongation. Thus, the expansion and contraction of the model do not occur out of the x-y plane ($\partial_z = 0$, $\theta_z = 0$).

For the BC3 established in the model, a reference point is constructed at the centre point of the cross-sectional area of another end. A coupling system is established for the whole cell coupling the cross-sectional area to the reference point (centre point), where the elongation (ΔL_x and ΔL_y) was applied. Thus, for uniaxial longitudinal stretch, the stretching is ΔL_{x1} and ΔL_{y1} for lateral stretch. The maximum elongation rate obtained experimentally is 7.78%, according to Table 1. To ease the calculation of the input values, the point that represents the whole end was subjected to stretching that caused the model to elongate with 10% strain which is equivalent to 9.5 mm elongation for longitudinal extension and 3 mm for lateral loading. Although the model in Figure

3 illustrated the implementation of straight pattern, the same boundary conditions were applied to different shape of ink patterns such as sinusoidal, zigzag and square.

2.4.2. Biaxial Loading

Another type of tensile loading is stretching the body or model on both x- and y-axis. This type of pulling is called biaxial tensile loading, where all ends of a square planar body/model are subjected to tensile load. In simpler words, biaxial loading combines both uniaxial longitudinal and lateral loading.

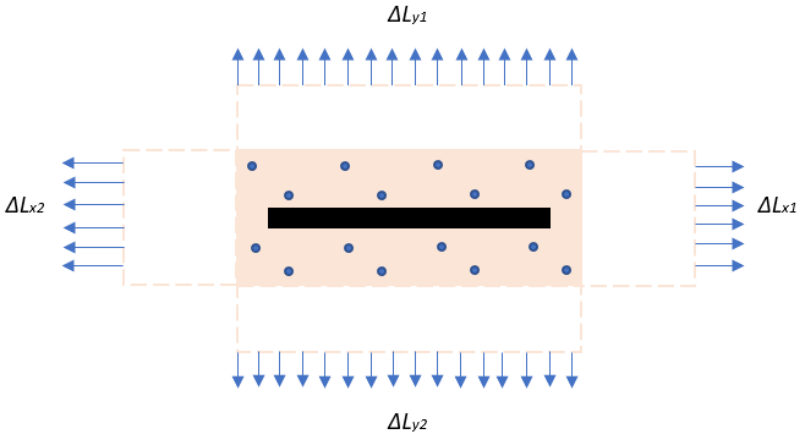

Figure 4. Applied boundary conditions for the model implementing the biaxial tensile loading. Just like uniaxial loading, dotted lines denoted the on the substrate denoted that the surface was constrained from deflection in z-axis while arrows indicated the loading point on each direction of the substrate.

Blue dots in the model are shown in Figure 4, denoting that the model was constrained from moving or displacing in the z-axis (out-of-plane) as it is free to deform in both x- and y-axis along with the applied elongation. Equation (3.0) until Equation (3.3) show the simplified tensile loadings applied onto each model implemented in this study. ΔL_{x1} and ΔL_{y1} represent the uniaxial longitudinal and lateral tensile loading. ΔL_x and ΔL_y represented the total stretching in the x-direction and y-direction, respectively. Biaxial tensile loading, ΔL_{total}, is denoted by Equation (1.5), where it is the sum of the total deformation of length in both longitudinal and lateral axis. The key difference between uniaxial and biaxial loading is that for the latter, tensile loading was applied in all directions compared to a single direction for uniaxial loading.

$$\Delta L_{x1} = \Delta L_{x2} = 1.5 \text{ mm} \quad (3.0)$$
$$\Delta L_{y1} = \Delta L_{y2} = 4.75 \text{ mm} \quad (3.1)$$
$$\Delta L_x = \Delta L_{x1} + \Delta L_{x2} = 3 \text{ mm} \quad (3.2)$$
$$\Delta L_y = \Delta L_{y1} + \Delta L_{y2} = 9.5 \text{ mm} \quad (3.3)$$
$$\Delta L_{total} = \Delta L_x + \Delta L_y = 12.5 \text{ mm}$$

2.4.3. Contact Properties Between Ink and Substrate

During the simulation, the surface of both ink and substrate are tied to each other through the master and slave-tie method, which is based on an assumption of no slipping between inks and

substrate's contact surface. In contrast, the silver ink is modelled as isotropic material possessing a linear elastic behaviour. Abaqus/CAE automatically gives master and slave designations to surfaces in a recognised contact pair. When mesh surfaces are assigned master and slave designations, rigid surfaces always become the master; if the contact pair has two rigid surfaces, the master and slave roles are assigned arbitrarily. Abaqus/CAE evaluates the mesh densities of the two deformable surfaces in contact pairs; the surface with the coarser mesh becomes the master surface. In this case, since the TPU substrate is more rigid than the silver ink, it was set as the master surface [16]. This explained the higher meshing density for TPU relatively to the silver ink since higher density contributed to a coarser mesh.

3. RESULTS AND DISCUSSION

3.1. Results of Mesh Convergence Study

Mesh convergence study in Figure 5 shows that the stress from the models is less than 10%, with the meshing density of the models set to be 0.7 and 1 for ink and substrate, respectively. Due to heavy computational workload leading to a lengthy simulation period, two patterns were chosen for the mesh convergence study. From past experimental work, straight pattern suffered the lowest conductivity after stretching while zigzag possessed the highest conductivity. Thus, these two patterns were chosen for this study to reduce the computational workload. For straight pattern, the value of maximum VMS began to stabilise as the element counts of the ink were increased to 517 elements, which resulted from the meshing density of 0.7 mm. In the case of the zigzag pattern, stabilisation of the maximum VMS occurred when the number of elements applied for simulation exceeded 1042, which, too, resulted in the meshing density of 0.7 mm. Thus, it can be said that for all patterns, the results obtained by the employment of meshing density of 0.7 mm or lower are sufficient to provide legit results. Lower mesh density for the straight design (0.5 mm) was employed solely to better match the number of elements with the other three remaining patterns. The number of nodes and elements of each pattern used generated from the mesh seed density of 0.7 is tabulated in Table 3. Post-validation, the model will be subjected to biaxial tensile load to further analyse the SCI model's behaviour under various mechanical loadings. For the validation purpose, the VMS and maximum principal strain for longitudinal tensile loading will be simulated and compared with the result obtained from the experimental works conducted as per Table 1. The distribution of both stress and strain resulting from the longitudinal tensile loading will be analysed and correlated with the findings from the past experimental work.

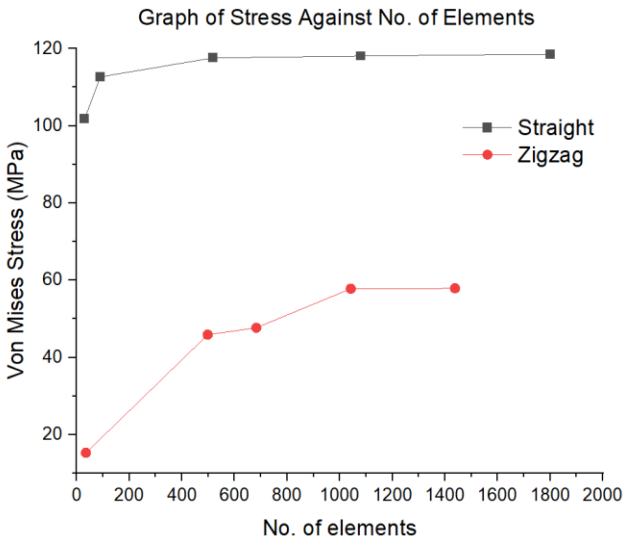

Figure 5. Graph of mesh convergence study for two patterns chosen; straight and zigzag

Table 3. Number of nodes and elements generated from the meshing results of each pattern

Pattern	Meshing Properties	
	No of nodes	No of elements
Straight	2534	1080
Square	2944	1222
Sinusoidal	2468	1002
Zigzag	2514	1042
Substrate	5952	2850

Table 4 shows the Von Mises Stress (VMS) obtained for all the patterns when subjected to uniaxial tensile loading of 10%.

Table 4. Tabulation of VMS for uniaxial longitudinal tensile loading of all the patterns

Pattern	Von Mises Stress (VMS) (MPa)		
	Maximum	Minimum	Average
Straight	118.143	65.760	91.952
Sinusoidal	63.134	9.185	36.160
Zigzag	57.826	11.354	34.590
Square	112.865	46.158	79.512

3.2. Maximum VMS Distribution on Patterns for Uniaxial Loading

3.2.1. Uniaxial Longitudinal Loading

The tabulated data obtained through the simulation process in Table 4 shows that the highest VMS occurred in a straight pattern, with the maximum stress captured at 118.143 MPa, followed by square, sinusoidal and zigzag patterns with 112.865, 63.134, and 57.826 MPa, respectively. For the sinusoidal line, the high concentration of stresses is located at various locations within the ink near the longitudinal centreline of the substrate (line of the half-width of the substrate), as shown in Figure 6(b). For straight ink, it is observed that the highest stress is accumulated in the middle of the ink with the stress value of 118.143 MPa, as the high-stress concentration covers up more than 90% of the ink surface. The stress concentration decreases as it approaches the longitudinal end of the straight ink, away from the centre of the pattern. High average stress distributed within the design contributed to the electrical conductivity's failure more than the localisation of high stress at a particular location within the conductive patterns. The high-stress value imposed on a large area of the straight ink pattern could incite the formation of more cracks within the silver ink's design, causing more defects; thus, the electron transfers are unable to move smoothly due to the scattering mechanism [1]. In Figure 6, take note that the stress contour for each stand-alone ink pattern is quite different compared to when observed at the whole system (ink on top of substrate). The stress contour of each ink pattern for the whole system illustrated a higher stress concentration due to each ink pattern suffered relatively higher concentrated stress compared to substrate. However, for a stand-alone ink pattern, the concentration of stress for each pattern was independent to the that of substrate as the substrate was 'hidden' to monitor the stress concentration of the ink directly. Thus, the stress indicator appeared in the left side of Figure 6 for each pattern was not applicable to the stress concentration for each of its stand-alone ink pattern. Hence, a slight difference in stress concentration between both systems can be seen. The same case was applied to each stress contour figure for each pattern onward.

As for the square ink pattern, higher stress accumulated at the outer edge of the square pattern. For the zigzag pattern, the maximum stress is distributed at the line closer to the outer edge of the zigzag pattern, with the highest stress recorded at 57.816 MPa. The FEA finding shows that the straight-line pattern induced the highest stress value at a more significant portion of the ink's surface when subjected to the uniaxial longitudinal tensile loading. As seen in Figure 6(b) until 6(d), other patterns exhibited a better distribution with a lower peak stress value than a straight-line pattern.

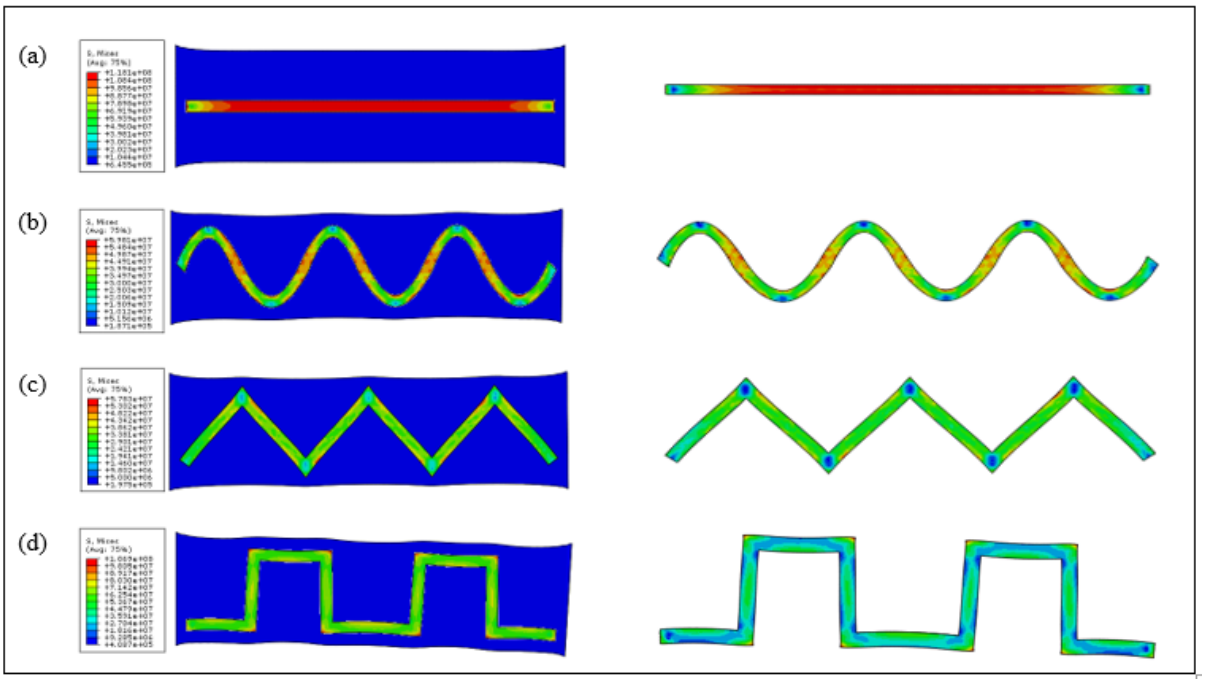

Figure 6. The stress distributions when subjected to uniaxial longitudinal tensile loading for (a) straight, (b) sinusoidal, (c) zigzag, and (4) square pattern, respectively

3.2.2. Validation of Results from Uniaxial Longitudinal Loading

The results of the maximum VMS imposed on different patterns of the ink fit the finding from the past research works referring to Table 1. It can be said that the higher the VMS imposed on the ink pattern resulting from the longitudinal stretch, the lower its ability to deform before losing its electrical conductivity. The lower the maximum VMS indicates the better stretchability of the patterns, which can be simplified as zigzag > sinusoidal > square > straight, and this sequence fits the finding from the experimental works from Table 1 conducted in the past where zigzag sustained higher stretching before electrical failure, followed by sinusoidal, square, and lastly straight pattern.

3.2.3. Uniaxial Lateral Loading

In contrast to the results in section 2.1, the model of patterns for this section is subjected to an elongation of 3 mm in the positive y-axis direction. The maximum VMS for all the patterns were recorded in Table 5. As illustrated, when the model is stretched laterally in the positive y-axis with another end fixed, it shows a different stress behaviour onto the patterns. One of the major differences is that unlike straight ink patterns experiencing the longitudinal stretching in which possessing the highest maximum stress, the same pattern under lateral tensile loading exhibited the lowest maximum stress relative to other patterns valued at 91.428 MPa. However, despite displaying the lowest maximum stress, the distribution of the high-stress value in the straight ink pattern is larger than other patterns, as seen in Figure 7.

In the case of uniaxial lateral tensile loading, the highest VMS occurred on the zigzag pattern at the tip of the outer edge of the first corner from the right with the stress value of 142.564 MPa.

Sinusoidal and square patterns possess the second and third highest VMS, respectively, valued at 138.781 and 128.51 MPa. From the result, although both zigzag and sinusoidal exhibit higher maximum stress compared to the straight and square pattern, their maximum stress is a localised stress value. For the zigzag pattern, the high-stress values are located at the tip of the outer edge of the zigzag corners, which is possessed by a single element for each of the tips. The observation is supported by Figure 8(a). Apart from these elements, the stress distribution for the zigzag pattern is reasonably low, averaging at 38.811 MPa, with the highest stress recorded at 59.800 MPa, which is much lower than other patterns' maximum stress value. The same can be said for the case of sinusoidal pattern, where high stresses are localised at the first crest on the left and first trough on the right (both viewed from the front). The maximum stress value for the sinusoidal pattern is 138.781 MPa which covers a tiny portion of the first crest from the left. By ignoring the small portion of the localised high-stress values, the new maximum stress value is 75.827 MPa, making it the second-lowest VMS among the patterns. Thus, although initially both of these patterns showcasing a higher maximum VMS compared to straight and square patterns, they can provide better electrical conductivity due to the localisation of the higher stress values causing the stress distribution to be more homogenous for low-stress concentration.

Table 5. Tabulation of VMS for uniaxial lateral loading of all the patterns

Pattern	Von Mises Stress (VMS) (MPa)		
	Maximum	**Minimum**	**Average**
Straight	91.428	40.337	65.883
Sinusoidal	138.781	14.614	76.698
Zigzag	142.564	17.822	80.193
Square	128.351	28.128	78.240

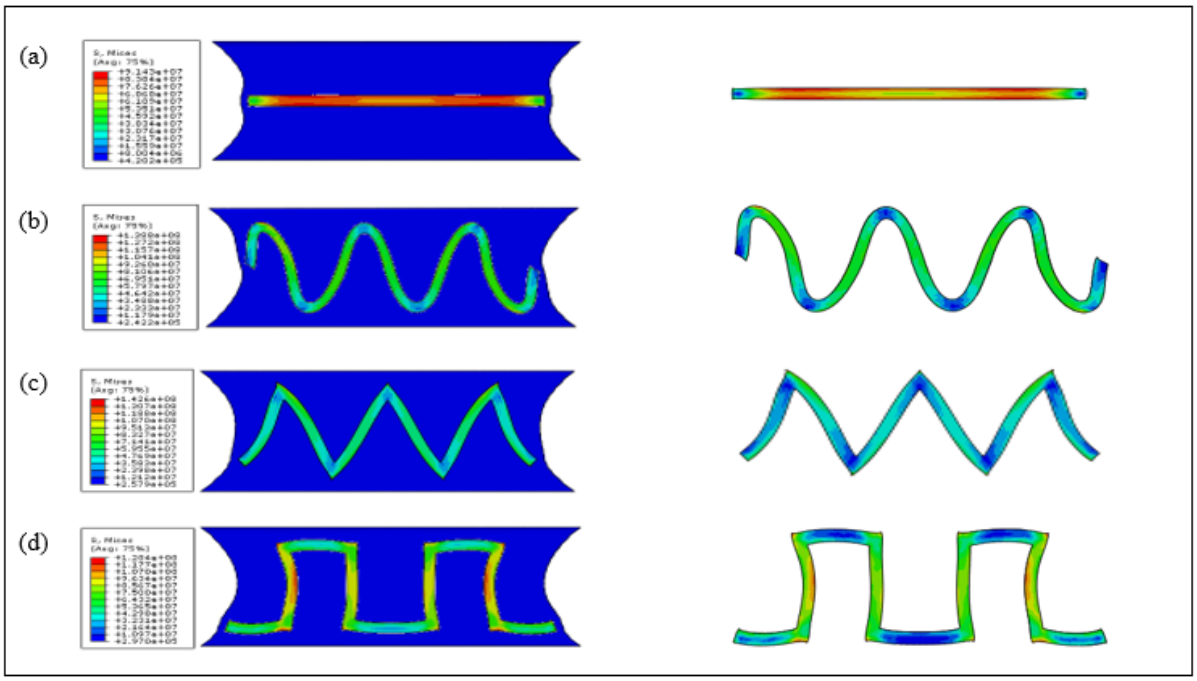

Figure 7. The stress distributions when subjected to uniaxial lateral tensile loading for (a) straight, (b) sinusoidal, (c) zigzag, and (4) square pattern, respectively

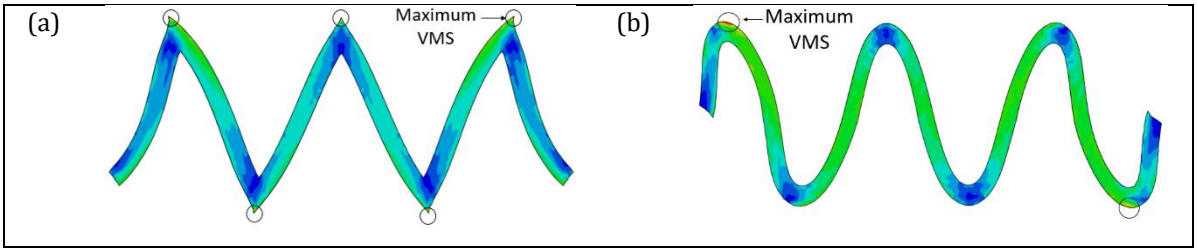

Fig. 8. (a) Localisation of high-stress value on zigzag ink pattern occurring at the tip of the outer edge of the zigzag pattern and (b) Localisation of high-stress value on sinusoidal ink pattern occurring at the tip of the outer crest and trough of the sinusoidal pattern

3.3. Maximum VMS Distribution on Patterns for Biaxial Loading

This section will observe and discuss the effect of stress distribution resulting from the biaxial tensile loading. Unlike the uniaxial tensile loading, which fixed one end of the model and loads applied at another end, models with different ink patterns incorporating the biaxial tensile loading will have all ends normal to both x- and y-axis applied with a tensile load. The VMS values and the VMS distribution of each pattern are tabulated and shown in Table 6 and Figure 9, respectively. According to Table 6, the zigzag pattern exhibited the highest VMS when subjected to biaxial tensile loading at 254.664 MPa, followed by sinusoidal, square, and straight patterns at 224.559, 169.996, and 82.817 MPa, respectively. The sequence is the total opposite of what was simulated for the case of uniaxial tensile loading.

To further analyse the recorded value, the location of the maximum VMS and the stress distribution for sinusoidal, zigzag, and square patterns are evaluated. The stress distribution of the different ink patterns is pictured within Figure 9, while the locations of the maximum VMS for straight, square, sinusoidal, and zigzag patterns are shown in Figure 10. Figure 10(b) until 10(d) shows that the maximum VMS is localised within a minimal area for square, sinusoidal, and zigzag patterns. For both zigzag and square patterns, the maximum VMS is possessed by a single element at the edge of the outer crest and end tip, respectively. When the element containing the maximum VMS is neglected, the new maximum VMS for the zigzag and square pattern is 92.729 and 103.445 MPa, respectively, which is still higher than that of the straight pattern. The same can be said for the sinusoidal pattern, at which the high-stress concentration is localised at the crest of the first corner of the ink from both left and right, with the maximum VMS recorded at 224.559 MPa. By ignoring the maximum VMS region, which is possessed by approximately 4 to 6 elements within the mesh, the new maximum VMS is 100.478 MPa which showcased a remarkable reduction of the stress.

Table 6. Tabulation of VMS for biaxial loading of all the patterns

Pattern	Von Mises Stress (VMS) (MPa)		
	Maximum	**Minimum**	**Average**
Straight	82.817	52.735	67.776
Sinusoidal	224.559	32.169	128.364

Zigzag	254.664	26.557	140.611
Square	169.996	26.694	98.345

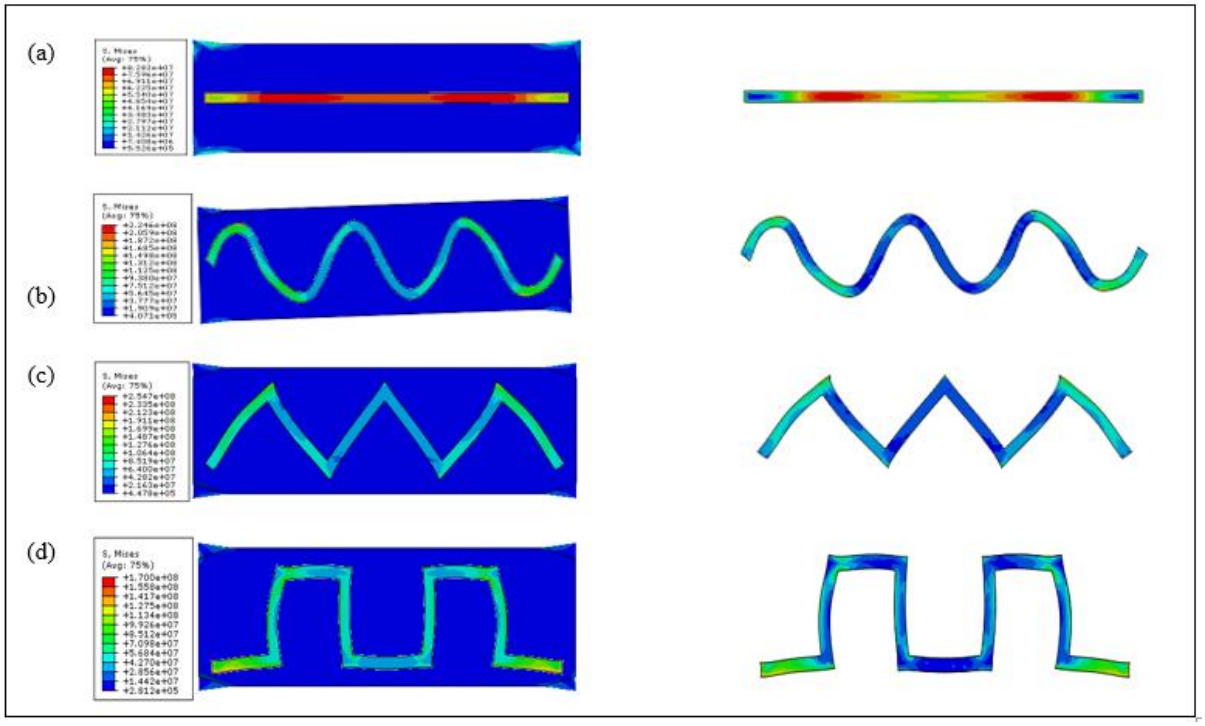

Fig. 9. The stress distributions when subjected to biaxial tensile loading for (a) straight, (b) sinusoidal, (c) zigzag, and (4) square pattern, respectively

Thus, for the analysis of the stress distribution on patterns for the biaxial tensile loading case, looking at both the new maximum VMS for each pattern after removing the localised initial maximum VMS and their average VMS value could propose a different perspective. This is because even though the maximum VMS of the straight pattern is lower than other patterns, the high-stress values were not localised at one point but distributed at a large scale on the ink pattern itself. This has caused the majority of the straight ink pattern to be subjected to a high-stress concentration, unlike any other patterns used in this study. Table 7 below tabulated the data for the new maximum VMS for each pattern subjected to the biaxial tensile loading. The square pattern has exhibited the highest VMS at 103.445 MPa, followed by sinusoidal, zigzag, and straight at 100.478, 92.729, and 82.817 MPa, respectively. However, a different scenario can be observed when the focus is shifted to the value of the average VMS. As tabulated below, the straight pattern has the highest average VMS at 67.776 MPa despite its lowest maximum stress value due to its relatively higher minimum VMS at 52.735 MPa. Once again, the zigzag pattern showcased an excellent distribution of relatively lower stress, as seen in Figure 9(c), supported by its low minimum VMS. In addition, it also exhibited a lower average VMS compared to other patterns. Thus, it can be said that even though initially zigzag pattern showed relatively higher maximum VMS, the majority of the surface area of the ink was covered with the lower stress concentration, and the stress value further reduced away from the point of applied loading.

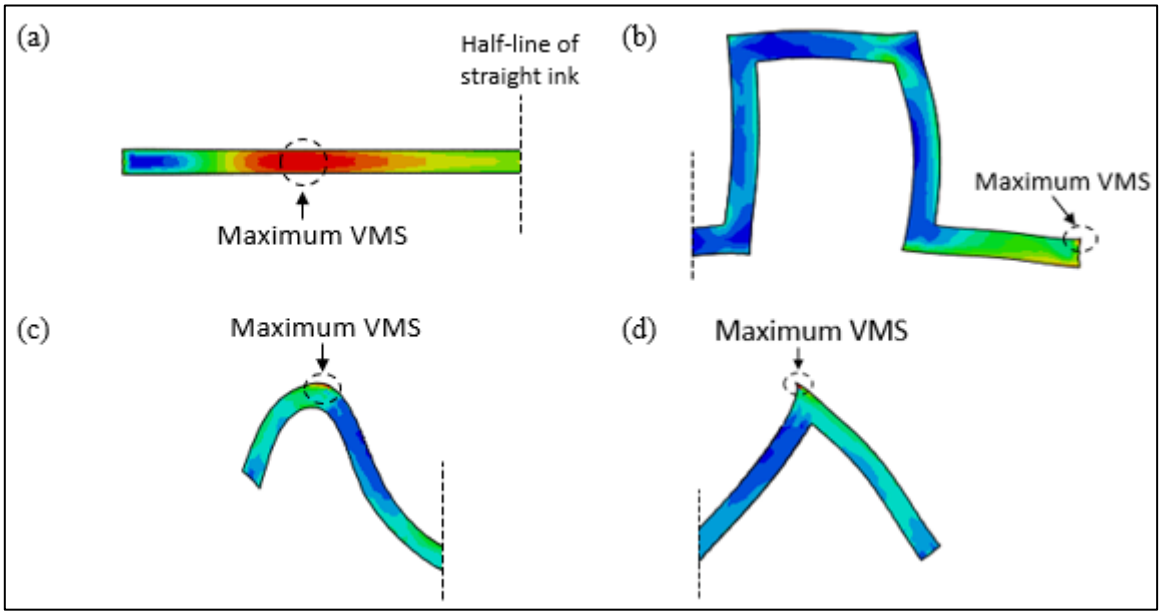

Fig. 10. The location of the occurrence of the maximum VMS for (a) straight, (b) square, (c) sinusoidal, and (d) zigzag pattern. The black dashed lines represent the cutting line for each pattern to simplify the model of the ink

Table 7. Tabulation of new VMS for biaxial loading of all the patterns

Pattern	Von Mises Stress (VMS) (MPa)		
	Maximum	**Minimum**	**Average**
Straight	82.817	52.735	67.776
Sinusoidal	100.478	32.169	66.324
Zigzag	92.729	26.557	59.643
Square	103.445	26.694	65.070

3.4. Maximum Principal Strain of Each Pattern for Uniaxial Loading

Maximum principal strain theory states that material failure will occur when the maximum principal strain developed within the material exceeds the limiting strain, which is the value corresponding to the yield point of the material. This section will evaluate the maximum principal strain of each of the patterns subjected to longitudinal, lateral, and biaxial loads. It is hypothesised that the lower maximum principal strain developed within a pattern will reduce the probability of the pattern failing, thus failing to conduct electricity.

3.4.1. Maximum Principal Strain for Uniaxial Longitudinal Loading

Apart from studying the VMS distribution on the different patterns when subjected to various types of tensile load, evaluating the level of maximum principal strain developed within a model is necessary. This is due to the assumption that the lower principal strain developed within a

body or the material will allow it to stretch more without failure [12]. The maximum principal strain obtained from the model of each pattern will be compared to the input strain, which is 10% for the case of uniaxial longitudinal tensile loading. The following Equation gives the percentage of the reduction of maximum principal strain:

$$\% \text{ Strain Reduction} = (E_i - \text{MPS}) / E_i \quad (3.0)$$

E_i is the input strain (10%), and MPS is the maximum principal strain for each pattern.

Table 8 shows the maximum principal strain for each pattern and their respective percentage of strain reduction. The straight pattern possessed the highest maximum principal strain from the tabulated result, marking at 10.39%. The exceeding of maximum principal strain that of straight ink pattern from the input of elongation strain has caused the value for its percentage strain reduction to become negative, indicating a bigger strain developed within the ink. Apart from the straight ink pattern, all patterns successfully reduce the development of the strain. The zigzag pattern has once again proven to offer the best stretchability as it showcased the highest percentage of strain reduction by 59.5%, followed by sinusoidal and square by 43.2% and 17.9%.

Table 8. Tabulation MPS and percentage of strain reduction for uniaxial longitudinal and lateral tensile loading of all the patterns

Pattern	Uniaxial Longitudinal Loading		Uniaxial Lateral Loading	
	Maximum Principal Strain (MPS)	Percentage Strain Reduction (%)	Maximum Principal Strain (MPS)	Percentage Strain Reduction (%)
Straight	10.39	-3.9	7.39	26.1
Sinusoidal	5.68	43.2	12.85	-28.5
Zigzag	4.05	59.5	13.95	-39.5
Square	8.21	17.9	12.51	-25.1

From the contour plots within Figure 11, it is observed that all of the ink patterns exhibited a lower maximum principal strain relatively that of their respective substrate, with an exception for the straight ink pattern. As seen, the strain distribution of the straight ink pattern is almost similar to that of the TPU substrate. For the stand-alone maximum principal strain distribution of the ink, the result for the straight pattern shows that a large principal strain is imposed on its surface. In contrast, other patterns significantly reduce strain ranging from 17.9% to 59.5% for three different patterns. From the uniaxial longitudinal loading, employing a different shape of the ink pattern, especially in meandering shapes such as sinusoidal and zigzag, may improve the stretchability due to the reduction of the local strain development within the ink. Straight ink pattern suffers from high maximum principal strain induced from elongation of 10%. On top of that, the majority of the area for the surface of the straight ink is covered by the high principal strain, which might be the main cause of failure to conduct electrical charge.

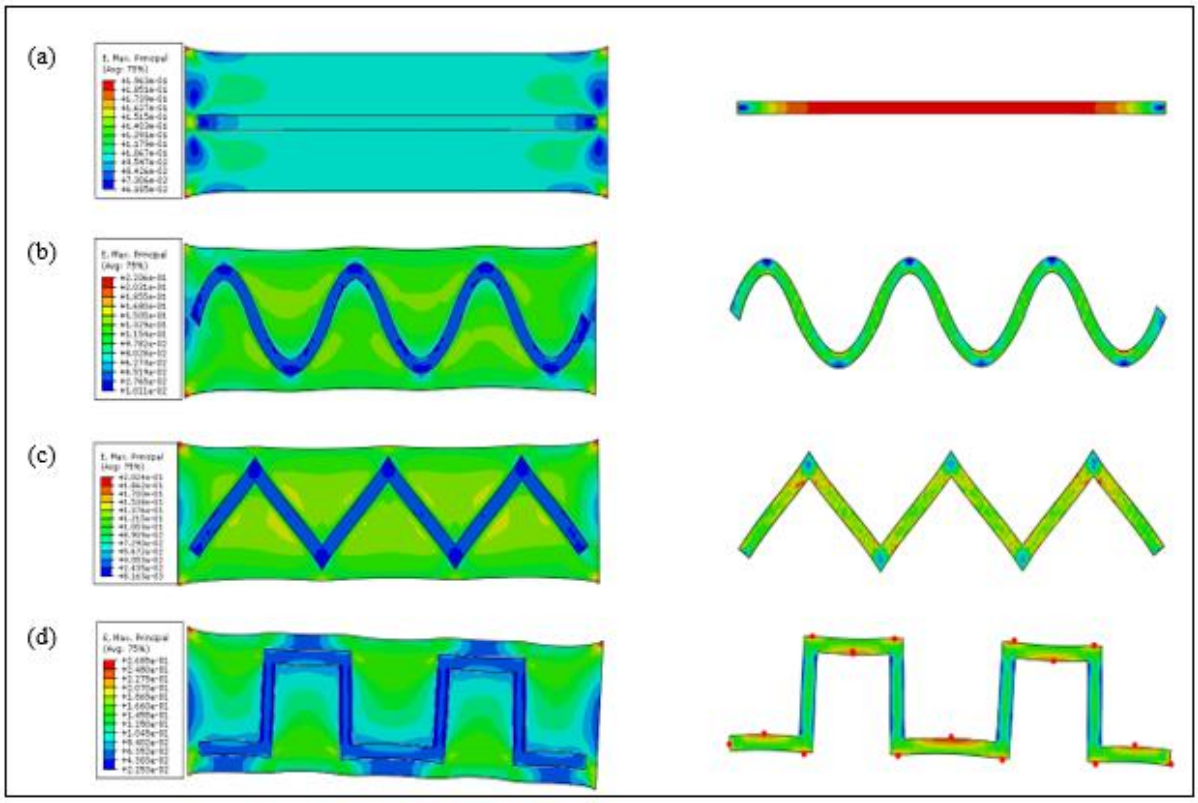

Fig. 11. Contour plot of the maximum principal strain distribution under uniaxial longitudinal tensile loading for the pattern of (a) straight, (b) sinusoidal, (c) zigzag, and (d) square. Figures on the left show the maximum principal strain on the whole model for each pattern, while figures on the right show the maximum principal strain of the stand-alone patterns

Figure 11 (d) describes the contour plot of the strain distribution within the square pattern—the red dots denoting the location of the high principal strain imposed during the 10% straining. For square pattern, results of maximum principal strain from FEA also show agreement with the experimental research [1], approving that the presence of a parallel-stretching zone in the intended structure is likely to contribute to the pattern's inability to tolerate a greater strain [1]. This is somewhat contradicting what Yunos et al. [1] mentioned through their study. From the FEA simulation, instead of high-stress concentration localised at the parallel-stretching zone for the square pattern, it was the localisation of high principal strain on that region that is observed to be the main contributor towards the failure mechanism of the square pattern.

3.4.2. Maximum Principal Strain for Uniaxial Lateral Tensile Loading

Table 8 shows the results of the maximum principal strain and the percentage of strain reduction for all the patterns subjected under uniaxial lateral tensile loading. The trend of the percentage of strain reduction for each pattern, this time, shows a different result in comparison to the same result for the uniaxial longitudinal loading. Surprisingly, straight patterns recorded a strain reduction of 26.1% under uniaxial lateral loading, while other remaining patterns suffered additional strain increment. For this case, the zigzag pattern suffers the highest strain increment of 39.5%, followed by sinusoidal and square at 28.5% and 25.1%, respectively. The negative values within the table indicate that instead of having a reduction of principal strain value, the pattern developed higher strain during stretching in comparison to the initial 10% elongation on

the end of the TPU substrate. Figure 12 depict the strain distribution for both the assembly and stand-alone ink for all the patterns. From the contour plot, despite having the lowest maximum principal strain, high strains developed within the ink of the straight pattern cover a larger area than other patterns. A clear finding for the uniaxial lateral loading is the major reduction in the strain accumulation within the straight ink model compared to that of uniaxial longitudinal loading. Unlike when it is subjected to longitudinal loading, under lateral loading, high principal strain is located at the edge of the top and bottom of the ink.

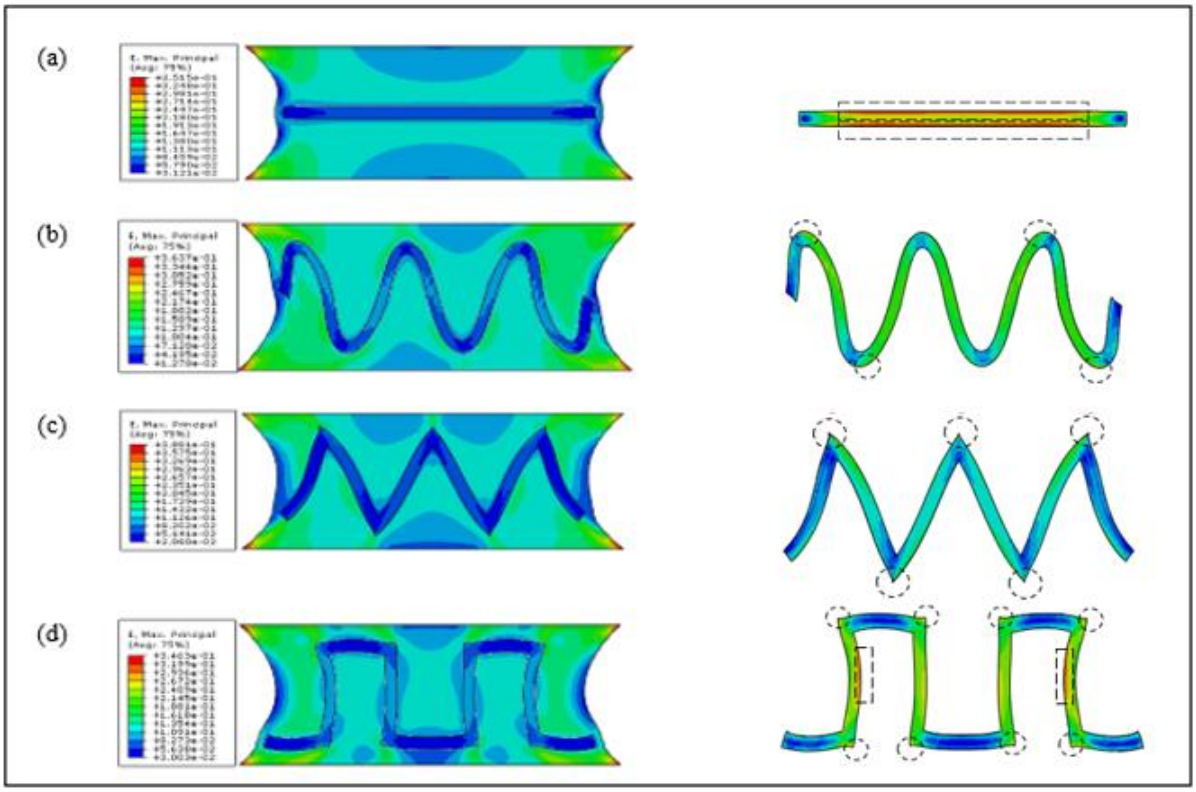

Fig. 12. Contour plot of the maximum principal strain distribution under uniaxial lateral tensile loading for a pattern of (a) straight, (b) sinusoidal, (c) zigzag, and (d) square. Figures on the left show the maximum principal strain on the whole model for each pattern, while figures on the right show the location of the high principal strain of the stand-alone patterns. Dotted circles indicated the high level of strain located at the tip while dotted rectangles indicated region of the high level of strain.

From the values tabulated for lateral loading, the employment of different shapes apart from straight patterns does not provide an additional advantage, in this case, in reducing the strain localisation. However, just like the case for the evaluation of Von Mises stress, the highest strains localisation appears to develop at just a few mesh elements, contradicting that of straight ink pattern. Figure 12 shows the location of the localised maximum principal strain for each pattern. High strain localisation for the straight pattern is distributed evenly at the top, and the bottom line of the ink with the highest strain value is marked at 7.39%. In this study, a straight pattern is more effective in reducing the strain localisation under the subjection to lateral loading compared to being subjected to the longitudinal loading. The much lower strain developed within the straight ink for the lateral loading than the longitudinal loading might be caused by the further distance between the ink pattern and the loading point. From the front view, for the case of lateral loading, the distance between the ink model and the point of applied loading is 13.5 mm and 2.5 mm for the longitudinal loading. For square pattern, the high-level strains are localised at the tip

of the outer edges of the ink ranging from 10.43% to 12.51%. Although the principal strain level is high at these points, the high level of strain is possessed by approximately three to seven elements with an area of 0.49 mm^2 each. Two areas parallel to straining (inside the dashed rectangular lines) also developed high principal strain values ranging from 9.23% to 11.43%. The contour plot in Figure 12(d) shows that higher strains are localised at the region parallel to the lateral loading.

For sinusoidal patterns, high principal strains are localised at the tip of four different regions, as shown in Figure 12(b), ranging from 9.96% to 12.85%. However, the high principal strain is developed within a minimal area, ranging from one to three small elements. By ignoring these elements, the average strain developed at the non-corner area (green area) is approximately 7.06% and 2.72% for the corner region. Thus, for the square pattern, the strain concentration for the whole ink pattern is relatively low despite having the highest maximum principal strain initially. The same condition can be explained for the zigzag pattern where the highest principal strains localised at the tip of the outer edge of the pattern. The strain at the tip of the edge ranges from 13.71% to 13.95%. The localised high strain is developed within one to three elements at the edge of the zigzag corner, while the strain concentration of the whole ink model by ignoring these high straining elements ranges from 2.08% to 7.028%. It can be concluded that for these two ink patterns, despite having high maximum principal strain initially, the average strain concentration within the model itself is relatively low.

3.5. Maximum Principal Strain of Each Pattern for Biaxial Loading

Table 9 tabulated the results for the maximum principal strain and percentage of strain reduction for all the patterns subjected to biaxial tensile loading. For biaxial loading, the model is subjected to 10% strain at all directions in the X-Y plane. Under biaxial loading, all the patterns do not exhibit any advantages from the different variations of patterns, as all the patterns are unable to reduce the magnitude of local strain. As tabulated, the straight pattern suffers the lowest increment of principal strain from the input elongation strain, with 6.8%, while the other three patterns exhibited far inferior values. Again, for straight patterns, the localisation of high magnitude of principal strain is distributed well on the region, as shown in Figure 13(a). The high magnitude of principal strains ranging from 9.69% to 10.75% covers more than 90% of the elements within the straight pattern. Thus, a straight ink pattern is assumed to be subjected to high straining due to the majority of the elements consisting of a large magnitude of local strains with an average strain magnitude of 10.22%.

Table 9. Tabulation of new MPS and percentage strain reduction for biaxial tensile loading of all patterns

Pattern	Maximum Principal Strain (MPS)	Percentage Strain Reduction (%)	New Average Principal Strain (%)	New Percentage Strain Reduction (%)
Straight	10.68	-6.8	10.22	-2.2
Sinusoidal	20.27	-102.7	8.70	13.0
Zigzag	18.08	-80.8	8.00	20.0
Square	19.69	-96.9	7.73	22.7

For sinusoidal patterns, the high magnitudes of principal strain are located in the area of rectangular dashed lines in Figure 13(b), where the values range from 18.51% to 21.83%. However, these magnitudes are possessed by a relatively very small number of elements compared to the total number of elements possessed by the ink model, which is approximately seven elements each. Thus, the localisation of the relatively much higher principal strain of these elements can be ignored since it is assumed that the higher principal strain magnitude will not significantly affect the model itself. By ignoring the magnitudes of these elements, a significant reduction in the local strain of the model can be observed, where the average principal strain of the model in the region of the dark blue dashed lines is 8.7%.

The same case is applicable to both zigzag and square patterns. Both inks also exhibited high magnitudes of local strain at a small region of the ink. Rectangular dashed lines in Figures 13(c) and 13(d) shows the location of high magnitudes of strain for both zigzag and square pattern, respectively. For the zigzag pattern, the maximum local strains are 24.35% and 24.45% for each location, possessing a single element each. Since the number of elements possessing this high magnitude of strain is so much lower than the total elements of the ink model, it is assumed that the high strain of these elements will not significantly affect the strain value of the whole model. The average strain concentration of the zigzag pattern within the blue dashed lines is approximately 8%, which is lower than both straight and sinusoidal patterns. As for the square pattern, the highest magnitudes of strain are located at the region of two red dashed lines of the edge tip of the horizontal lines. The range of the high local strains is around 15.01% to 20.08% in these regions. However, similar to sinusoidal and zigzag patterns, the outstandingly high local strain is developed within just a few elements ranging from seven to ten elements per region. By ignoring these elements, the range of the local strains for regions A and B are approximately 5.24% to 13.83%, and the average strain magnitude is approximately 7.73%. It can be said that varying the shape of the ink conductor may improve the magnitude of local strain for each of the patterns under the biaxial tensile loading.

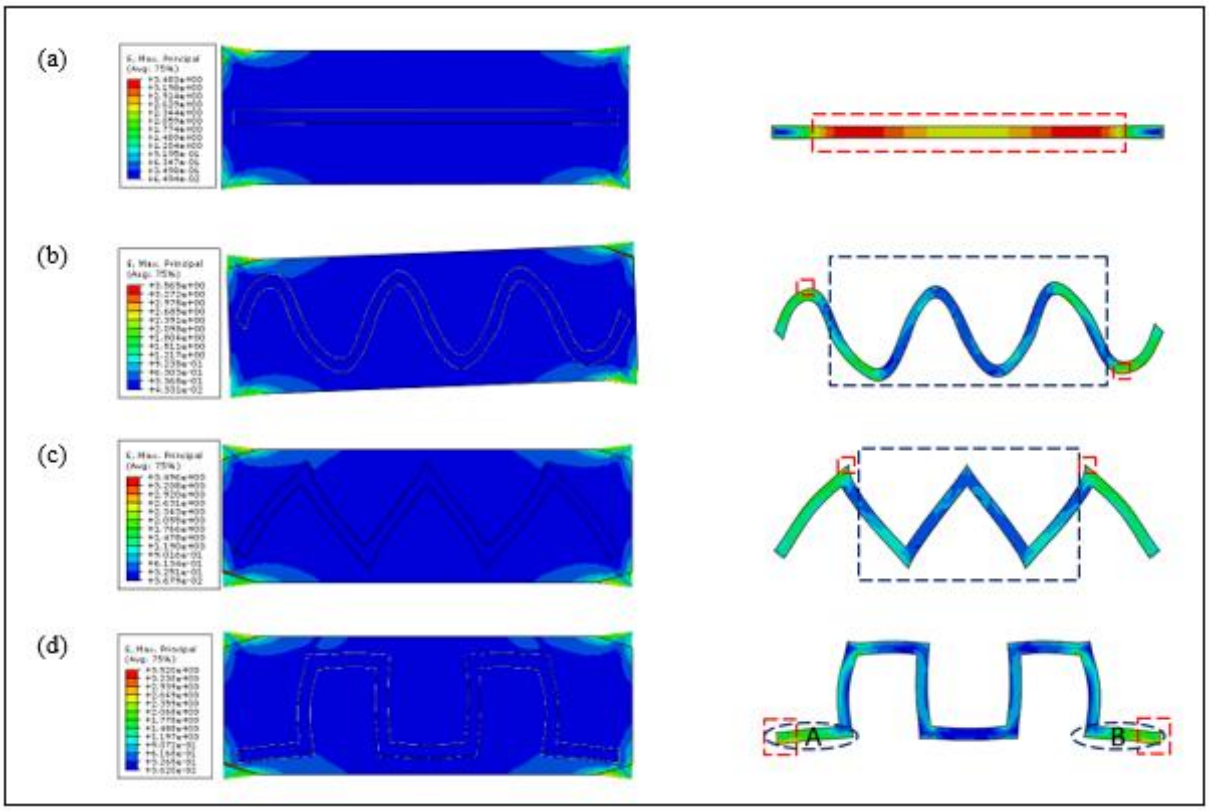

Fig. 13. Contour plot of the maximum principal strain distribution under biaxial tensile loading for a pattern of (a) straight, (b) sinusoidal, (c) zigzag, and (d) square. Figures on the left show the maximum principal strain on the whole model for each pattern, while red-dashed lines from figures on the right show the location of the high magnitude of principal strain for the stand-alone patterns. Blue dashed lines represent the region with relatively lower local strain magnitudes

4. CONCLUSION

In summary, a study incorporating the FEA method by Abaqus has been conducted to validate the effect of stress and strain distribution on the electrical performance of the silver-filled SCI by evaluating the stress and strain distribution of each pattern subjected to various types of loading. From the study, it can be concluded that maximum VMS and maximum principal strain played a significant role in determining the electrical performance of silver SCI subjected to uniaxial tensile loading with a 10% strain rate incorporated for the simulation process. Uniaxial lateral and biaxial tensile loading is subjected to each of the different ink patterns to further study each pattern's stress and strain distribution at varying types of loading. By aligning the results from the simulation relatively to that of experiment, it can be concluded that the lowest maximum VMS and principal strain contributed to a better electrical performance of SCI and better stretchability. This might be due to the appearance of lesser cracks within the SCI, allowing the electron transfers to be efficiently conducted. From both experiment and simulation conducted, it can be summarised that the electrical performance of different patterns of silver ink subjected to straining can be indicated as zigzag > sinusoidal > square > straight line. Some suggestions that may be recommended for further works are to consider the development of the plastic strain within the model as it is believed to play a significant role in influencing the stretchability of the designs [17], [18]. Out-of-plane simulation should also be considered. It may induce different stress concentrations at the centre due to the small crumpling and bending effect onto the model

[19]. Future works include implementing hyperelastic and plastic behaviour onto each TPU substrate and SCI, respectively, as it was cited to provide higher accuracy of the stress-strain curve compared to experimental works [20], [21]. This study may provide an insight on how the failure mechanism of stretchable electronic circuit used in application such as thermo-sensor under applied stress and strain.

ACKNOWLEDGEMENTS

The authors would like to express gratitude to Universiti Teknikal Malaysia Melaka for the UTeM Zamalah Scheme Scholarship, the Ministry of Education (MoE), Malaysia, under grant no. INDUSTRI(CREST)/TOPEMPIRE/2021 /FKM/100053, Collaborative Research in Engineering, Science and Technology Centre (CREST) and Advanced Material Characterization Laboratory (AMCHAL) make this study possible. Special thanks to Assoc. Prof. Dr Mariam Binti Md Ghazaly from the Department of Mechatronics Engineering for providing an Abaqus license, thus allowing this study to happen.

REFERENCES

[1] Yunos, A., M., Omar, G., Hamid, H., A., Salim, M., A., Masripan, N., A. The influence of geometrical dimensions on electromechanical performance in stretchable circuit. J. Phys. Sci. vol **31**, issue 2 (2020) pp.75–89.

[2] Gupta, S., Heidari, H., Vilouras, A., Lorenzelli, L., Dahiya, R. Device Modelling for Bendable Piezoelectric FET-Based Touch Sensing System. IEEE Trans. Circuits Syst. I Regul. Pap. vol **63**, issue 12 (2016) pp.2200–2208.

[3] Bossuyt, F., Vervust, T., Vanfleteren, J. Stretchable Electronics Technology for Large Area Applications : Fabrication and Mechanical Characterization. vol **3**, issue 2 (2013) pp. 229–235.

[4] Mou, Y., Zhang, Y., Cheng, H., Peng, Y., Chen, M. Fabrication of highly conductive and flexible printed electronics by low temperature sintering reactive silver ink. Appl. Surf. Sci. vol **459**, issue May (2018) pp.249–256.

[5] Mohammed A., Pecht, M. A stretchable and screen-printable conductive ink for stretchable electronics. Appl. Phys. Lett. vol **109**, issue 18 (2016).

[6] Kim, D., S., Jeong, J., M., Park, H., J., Kim, Y., K., Lee, K., G., Choi, B., G., Highly Concentrated, Conductive, Defect-free Graphene Ink for Screen-Printed Sensor Application. Nano-Micro Lett. vol **13**, issue 1 (2021).

[7] Xu, L., Y., Yang, G., Y., Jing, H., Y., Wei, J., Han, Y., D. Ag-graphene hybrid conductive ink for writing electronics Nanotechnology. vol **25**, issue 5 (2014).

[8] Suhaimi, M., A., Akop, M., Z., Azmi, M., Z., Rozali, N., S., Sobri, N., H, Nadlene, R., Azli, S., A., Salim, M., A., Mansor, M., R., Fadzullah, S., H., M., H., Effect type of conductive inks to stretchable printed circuit under thermal performance. issue May (2018) pp.279–280

[9] Ashikin, A., A., Omar, G., Tamaldin, N., Nordin, M., A., Akop, M., Z. Electrothermal Effects of Stretchable Conductive Ink (SCI). pp.18–19.

[10] Kosmala, A., Wright, R., Zhang, Q., Kirby, P. Synthesis of silver nano particles and fabrication of aqueous Ag inks for inkjet printing. Mater. Chem. Phys. vol. **129**, issue 3 (2011) pp.1075–1080.

[11] E. J. Hearn, " Mechanics of Materials 2: An Introduction to the Mechanics of Elastic and Plastic Deformation of Solids and Structural Materials," Ed 3. Eastbourne, Great Britain: Anthony Rowe Ltd, (2001) pp. 300-301.

[12] Kim, K., Y., Lee, C., J., Jung, S., B. Design and analysis of Cu circuit for stretchable electronic

circuits using finite element analysis. Microelectron. Eng., vol **238**, issue January (2021) p. 111510.

[13] Gonzalez, M., Axisa, F., Vanden Bulcke, M., Brosteaux,D., Vandevelde, B., Vanfleteren, J. Design of metal interconnects for stretchable electronic circuits. Microelectron. Reliab., vol **48**, issue 6 (2008) pp.825–832, 2008.

[14] Ab Wahid, A., K., Salim, M., A., Ali, M., Masripan, N., A., Dai, ., Md. Saad, A. Measurement of optimal stretchability graphene conductive ink pattern by numerical analysis. (2018) pp.43–54.

[15] A. Khennane, "Introduction to Finite Element Analysis Using MATLAB and Abaqus," Ed 1. Florida, United States: Taylor & Francis Group, (2013) pp. 141-142.

[16] Dassault Systèmes Simulia, "Abaqus CAE User's Manual (6.12)," Manuals, (2012) pp. 15-18.

[17] Yang, J., K., Lee, Y., J., Yi, S., M., Kim, B., J., Joo, Y., C. Effect of twisting fatigue on the electrical reliability of a metal interconnect on a flexible substrate. J. Mater. Res. vol. **33**, issue 2 (2018) pp.138–148.

[18] Ye, C. Stewart, B., G., Sitaraman, S., K. Stretchability of Serpentine Interconnect on Polymer Substrate for Flexible Electronics: A Geometry and Material Sensitivity Analysis. Proc. - Electron. Components Technol. Conf. issue June (2020) pp.1533–1541.

[19] Li, M., Torah, R., Liu, J., Tudor, J., Beeby, S. Finite element analysis (FEA) modelling and experimental verification to optimise flexible electronic packaging for e-textiles. Microsyst. Technol. (2020).

[20] Norhidayah, A., A., Saad, A., A., Sharif, M., F., M., Ani, F., C., Ali, M., Y., T., Ibrahim, M., S., Ahmad, Z. Stress Analysis of a Stretchable Electronic Circuit. Procedia Eng. vol. **184** (2017) pp.625–630.

[21] Aziz, N., A., Saad, A., A., Ahmad, Z., Zulfiqar, S., Ani, F., C., Samsudin, Z. Stress analysis of stretchable conductive polymer for electronics circuit application. Handb. Mater. Fail. Anal. issue April (2020) pp.205–224.